

# Strain-induced orbital-energy shift in antiferromagnetic RuO<sub>2</sub> revealed by resonant elastic x-ray scattering

Benjamin Z. Gregory,<sup>1,2</sup> Jörg Strempler,<sup>3</sup> Daniel Weinstock,<sup>2</sup> Jacob P. Ruf,<sup>1,4</sup> Yifei Sun,<sup>2</sup> Hari Nair,<sup>2</sup> Nathaniel J. Schreiber,<sup>2</sup> Darrell G. Schlom,<sup>2,5,6</sup> Kyle M. Shen,<sup>1,5</sup> and Andrej Singer<sup>2</sup>

<sup>1</sup>Laboratory of Atomic and Solid State Physics, Department of Physics, Cornell University, Ithaca, New York 14853, USA

<sup>2</sup>Department of Materials Science and Engineering, Cornell University, Ithaca, New York 14853, USA

<sup>3</sup>Advanced Photon Source, Argonne National Laboratory, Lemont, Illinois 60439, USA

<sup>4</sup>Max-Planck Institute for Chemical Physics of Solids, Nöthnitzer Straße 40, 01187 Dresden, Germany

<sup>5</sup>Kavli Institute at Cornell for Nanoscale Science, Cornell University, Ithaca, New York 14853, USA

<sup>6</sup>Leibniz-Institut für Kristallzüchtung, Max-Born-Straße 2, 12489 Berlin, Germany



(Received 21 January 2022; revised 21 October 2022; accepted 25 October 2022; published 18 November 2022)

In its ground state, RuO<sub>2</sub> was long thought to be an ordinary metallic paramagnet. Recent neutron and x-ray diffraction revealed that bulk RuO<sub>2</sub> is an antiferromagnet with  $T_N$  above 300 K. Furthermore, epitaxial strain induces superconductivity in thin films of RuO<sub>2</sub> below 2 K. Here, we present a resonant elastic x-ray scattering study at the Ru  $L_2$  edge of the strained RuO<sub>2</sub> films exhibiting the strain-induced superconductivity. We observe an azimuthal modulation of the 100 Bragg peak consistent with bulk. Most notably, in the strained films displaying superconductivity, we observe a  $\sim 1$  eV shift of the Ru  $e_g$  orbitals to a higher energy. The energy shift is smaller in thicker, relaxed films and films with a different strain direction. Our results provide further evidence of the utility of epitaxial strain as a tuning parameter in complex oxides.

DOI: [10.1103/PhysRevB.106.195135](https://doi.org/10.1103/PhysRevB.106.195135)

The ruthenium-based oxides host a rich set of physical phenomena, including unconventional superconductivity in Sr<sub>2</sub>RuO<sub>4</sub> [1], metamagnetic quantum criticality in Sr<sub>3</sub>Ru<sub>2</sub>O<sub>7</sub> [2–4], antiferromagnetism in both the Mott insulator Ca<sub>2</sub>RuO<sub>4</sub> [5] and in the strongly correlated metal Ca<sub>3</sub>Ru<sub>2</sub>O<sub>7</sub> [6,7], and both paramagnetic and ferromagnetic metallic states in CaRuO<sub>3</sub> and SrRuO<sub>3</sub>, respectively [8]. Ruddlesden-Popper ruthenates undergo a variety of electronic, magnetic, and orbital ordering transitions, which are tunable with chemical doping, pressure, temperature, magnetic field, and epitaxial strain [9]. In the ruthenium-based superconductor Sr<sub>2</sub>RuO<sub>4</sub>, uniaxial pressure has been shown to increase  $T_c$  [10] and epitaxial strain can alter the topology of its Fermi surface [11]. Uniaxial pressure has additionally been shown to induce a paramagnetic to ferromagnetic transition in Sr<sub>3</sub>Ru<sub>2</sub>O<sub>7</sub> [12] and epitaxial strain can enhance the existing magnetization in ferromagnetic SrRuO<sub>3</sub> [13,14].

A particularly striking example in this vein is the recent creation of a superconductor with epitaxial strain from non-superconducting RuO<sub>2</sub> [15,16]. Bulk RuO<sub>2</sub> has a rutile crystal structure (space group no. 136,  $a = 4.492$  Å,  $c = 3.106$  Å) at room temperature (295 K). Ruf *et al.* [15] reported strain-induced superconductivity in RuO<sub>2</sub> films, synthesized via molecular-beam epitaxy (MBE) on isostructural TiO<sub>2</sub> substrates ( $a = 4.594$  Å,  $c = 2.959$  Å) of differing surface orientations: TiO<sub>2</sub> (110) and TiO<sub>2</sub> (101). The superconducting ground state below 2 K is only present in the (110)-oriented films while the (101)-oriented films remain metallic. On TiO<sub>2</sub> (101) the lattice mismatch of the sample and substrate imparts in-plane tensile strain of +0.04% along  $[\bar{1}01]$  and +2.3%

along  $[010]$ . In the (110)-oriented sample the strain is compressive (−4.7%) along  $[001]$  and tensile (+2.3%) along  $[\bar{1}\bar{1}0]$ . The unit cells including strain directions are shown in Figs. 1(a) and 1(b).

In addition to its unexpected superconductivity, RuO<sub>2</sub> was long thought to be an ordinary, metallic paramagnet [17], but recent neutron diffraction results support an antiferromagnetic (AFM) ground state with spins aligned along the  $c$  axis with a Néel temperature,  $T_N$ , greater than 300 K [18]. Further resolution of the magnetic ordering is experimentally accessible through resonant elastic x-ray scattering (REXS) [19,20]. Azimuthal analysis of REXS (rotating the sample around the scattering vector) at the Ru  $L_2$  edge in bulk RuO<sub>2</sub> supports the existence of AFM ordering with moments largely along the  $c$  axis but with canting toward the  $a$ - $b$  plane [21]. This canted AFM conclusion has been questioned in subsequent work [22], though nonscattering techniques based on antiferromagnetic spin Hall effect offer further support for an antiferromagnetic origin of this signal [23]. In this paper, we use REXS to study the effect of epitaxial strain on the antiferromagnetism in strained films that display strain-stabilized superconductivity [15]. We provide further analysis of the strain-dependent phenomenology of these samples, using “sc110” and “ns101” as shorthand for the superconducting (110)-oriented sample (thickness 21.0 nm) and the nonsuperconducting, (101)-oriented sample (thickness 18.6 nm), respectively. Electrical and structural characterization for both samples is provided in the Supplemental Material [24] (see also Refs. [15,18,21,25] therein).

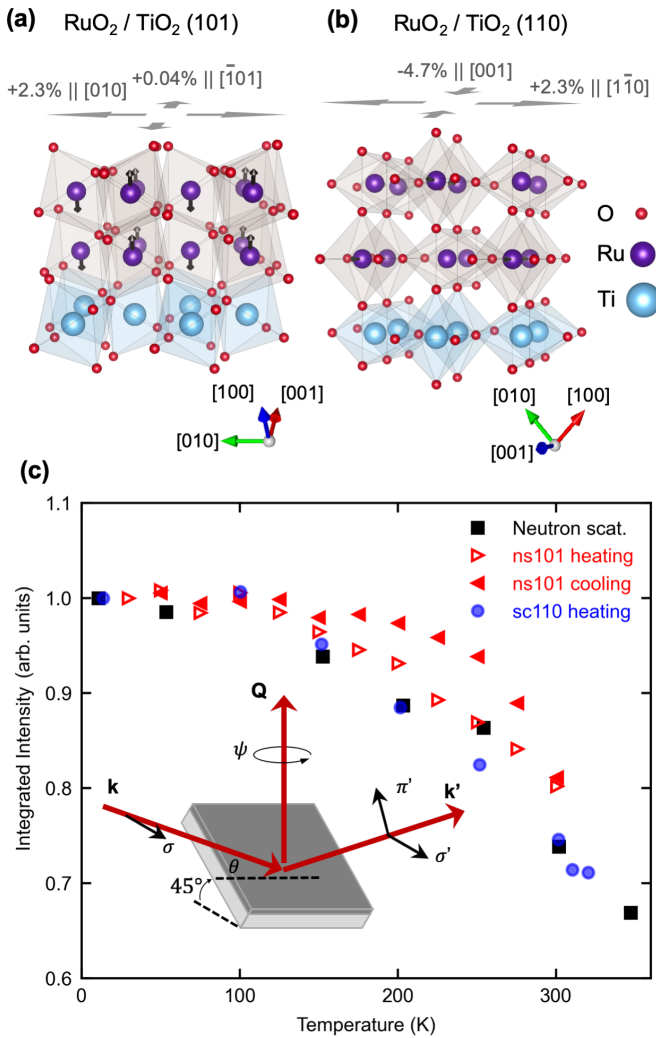


FIG. 1. Resonant magnetic scattering from strained  $\text{RuO}_2$  thin films. (a) Crystal structure of  $\text{RuO}_2$  with in-plane strains (gray arrows) synthesized on  $\text{TiO}_2(101)$  substrate. (b) Same as (a) with  $\text{TiO}_2(110)$  substrate. The short names ns101 and sc110 label the nonsuperconducting (101)-oriented sample and the superconducting (110)-oriented film, respectively. The substrate surface normal is oriented toward the top of the page, the magnetic moments (black arrows) of the Ru atoms are aligned along the  $c$  axis for clarity. (c) Depicts the temperature dependence of the integrated magnetic 100 Bragg peak. The black squares show the magnetic ordering temperature dependence obtained by neutron scattering, redrawn from Ref. [18]. The inset illustrates the resonant scattering geometry, where  $\theta$  is the incident angle,  $\mathbf{k}$  is the x-ray wave vector,  $\mathbf{Q}$  is the scattering vector, and  $\psi$  is the azimuth measured around  $\mathbf{Q}$ . Photon polarization orthogonal to the scattering plane is denoted  $\sigma$ , in-plane is denoted  $\pi$ . The  $45^\circ$  tilt is required for accessing the 100 reflection and severely constrains access to Bragg peak as  $\psi$  varies.

To investigate the effect of large epitaxial strain on the magnetic ground state of the  $\text{RuO}_2$ , we performed resonant magnetic x-ray scattering at the Ru  $L_2$  edge (2.968 keV) at beam line 4-ID-D of the Advanced Photon Source at Argonne National Laboratory [see inset in Fig. 1(c) for the scattering geometry]. On resonance, superlattice peaks or structurally forbidden peaks appear corresponding to charge, spin, or orbital ordering. The polarization and azimuthal dependences of

these forbidden reflections have already provided refinement of the ordered phases in ruthenates [21,26–30]. We tuned the x-ray scattering geometry to the structurally forbidden 100 Bragg peak, shown to be sensitive to the AFM order [21]. Because of the vertical scattering geometry without polarization analysis, we are averaging the scattered intensity in the  $\sigma-\pi'$  and  $\sigma-\sigma'$  channels. Figure 1(c) shows the normalized, integrated 100 peak intensity as a function of temperature for both strain orientations, upon cooling and heating. In addition, we have redrawn the original neutron scattering data from 2017 in the same plot [18]. Among all of these measurements, we observe general agreement in the temperature dependence, with a small discrepancy between the ns101 heating and cooling data. As neutrons offer a direct probe of magnetic order, we interpret the agreement of the temperature dependence measured here with the neutron data in bulk as further confirmation of the antiferromagnetic origin of the forbidden peak as opposed to another anomalous scattering mechanism.

Figures 2(a) and 2(b) show a width comparison of the structurally allowed 200 Bragg reflection and the structurally forbidden magnetic 100 Bragg reflection orthogonal to the scattering vector measured while rocking the incident angle  $\theta$  [see inset in Fig. 1(c)]. To access the 100 and 200 peaks, we tilted both samples' normal vectors to 45 degrees with respect to the scattering plane, shown in the inset to Fig. 1(c). Due to the differing sample orientations, the peak widths in ns101 and sc110 correspond to correlation lengths along the [010] and [001] directions. In both films, the magnetic peak is broader than the structural peak. Assuming minimal mosaicity as a result of epitaxial growth, we attribute the broadening to the finite coherence length of the probed region, suggesting the presence of multiple magnetic subdomains present in each coherent crystalline domain. We quantify this analysis by estimating the size of the crystalline coherent (charge) domains and the magnetic domains from the full width at half maximum (FWHM) of the Bragg peaks. These estimates provide a lower bound on the domain sizes, whose estimated size would grow if mosaicity were accounted for. In ns101, we estimate the structural and magnetic domains to be around 710 and 230 nm along the [010] direction, respectively. In sc110, we estimate the structural and magnetic domains to be around  $2.6 \mu\text{m}$  and 460 nm along [001], respectively. We thus find that each crystalline coherent domain contains three to five antiferromagnetic domains on average. Additionally, we observe that both the 100 and 200 peaks are broader in the ns101 film. The smaller peak widths in the film under higher strain, sc110, are surprising, yet this trend is consistent with the rocking curve measurements of specular reflections in both samples shown in Supplemental Material Fig. 3 of Ref. [15].

To determine if the different strain states change the orientation of the magnetic moments, we studied the azimuthal dependence of the magnetic Bragg reflection by measuring the integral intensity of the 100 peak while rotating the specimen around the momentum transfer vector  $\mathbf{Q}$  by the azimuthal angle  $\psi$  ( $\psi = 0^\circ$  when [001] lies in the scattering plane). The scattering geometry [see Fig. 1(c)] severely restricted the accessible azimuthal range, allowing only  $\sim 25^\circ$  of rotation before the sample eclipsed the incident or diffracted x-ray beam. When the sc110 sample is in the right scattering geometry to access 100, the  $c$  axis lies in the scattering plane,

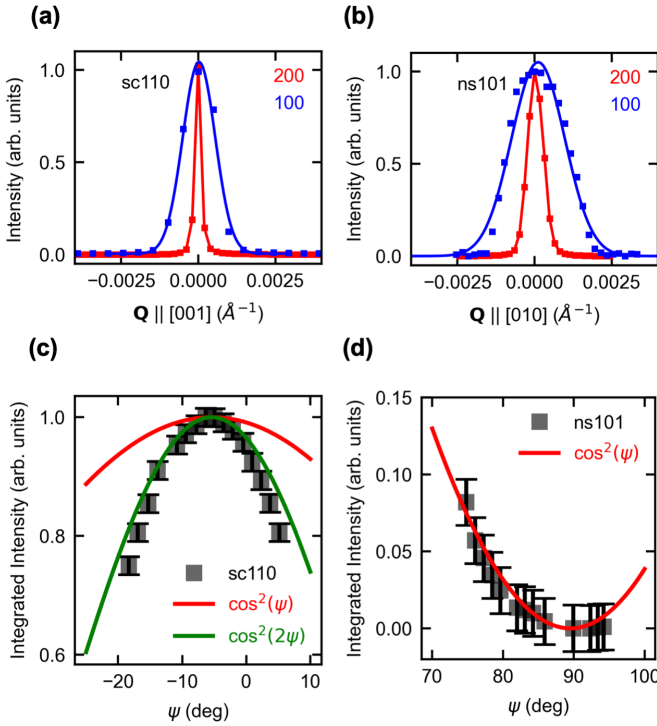


FIG. 2. Antiferromagnetic ordering and azimuthal dependence of the magnetic reflection. Panels (a) and (b) show the structural Bragg peak 200 (red) and the magnetic Bragg peak 100 (blue) of the (110)-oriented (sc110) and (101)-oriented (ns101) samples, respectively. The 100 peaks were measured at 2.968 keV and the 200 peaks at 5.936 keV without readjustment. Solid lines are best Gaussian fits. All peaks are normalized to 1. Panel (c) shows the integrated intensity of the 100 peak as a function of the azimuth from the sc110 sample; the data are the average of two repeated measurements over the same angular range, rescaled to a maximum value of 1.0 and corrected for absorption and volume illuminated. The error bars show the average standard deviations in the data over all  $\psi$ ; the same errors are assumed in (d).  $\psi = 0$  occurs when the crystallographic  $c$  axis lies in the scattering plane. The red curve is the theoretical fit for magnetization purely along  $c$  axis [Eq. (2) in main text]; green is the additional  $\cos^2(2\psi)$  term [Eq. (3) in main text], both shifted by  $\delta = -5.4^\circ$ . (d) Same as in (c) for the ns101 sample. The data represent a single scan with intensity rescaled so that its extrapolated maximum value at  $\psi = 0^\circ$  is 1.0 when fit with  $\cos^2(\psi)$  (red curve) in order to assume the same uncertainties measured in sc110.

but to achieve the same Bragg condition in ns101, the  $c$  axis points orthogonal to the scattering plane. Thus, in our azimuthal measurements we are able to access the region around  $\psi = 0^\circ$  in sc110 and around  $\psi = 90^\circ$  in ns101. Due to the scattering geometry (specifically that  $\psi$  is around  $90^\circ$  in ns101; see Fig. 2), the REXS intensity from ns101 is much lower than that of sc110, and it may be that the scattering is sensitive to a small, unknown hysteretic effect that only appears when magnetic scattering signal is weak. For example, a small change in the magnetic moment direction upon heating or cooling would show a larger percentage change of integrated intensity when the intensity is close to zero, a possible explanation of the anomaly in the ns101 temperature dependence in Fig. 1. Nevertheless, Figs. 2(c) and 2(d) both display azimuthal modulation of the integral intensity,

normalized by the integrated structural peak 200 at the same azimuth and corrected for self-absorption due to varying path length, in epitaxial films comparable to that measured in bulk  $\text{RuO}_2$  [21], a further indication of the superb film quality and the absence of twinning in our samples.

The simplest model of resonant magnetic scattering consists of a magnetic moment in spherical symmetry with fixed incoming and outgoing, linear polarization. The leading contribution to the intensity of such a scattering process is [31]

$$I \propto |\mathbf{e} \times \mathbf{e}' \cdot \hat{\mathbf{m}}|^2, \quad (1)$$

where epsilon and epsilon' are the polarizations of the incoming and scattered x-rays, and  $\mathbf{m}$  is the magnetization unit vector. We first assume that the magnetic moment lies along the  $c$  axis [16,24] and consider the orthorhombic ( $D_{2h}$ ) crystal field around the Ru atom. In this case without canting ( $\hat{\mathbf{m}} = [001]$ ), the scattering tensor reduces to the same form as that in spherical symmetry [19]. We first analyze the sc110 data. After rescaling the amplitude to 1.0 and including an offset,  $\delta$ , to account for possible sample misalignment and capture azimuthal shifts of physical origin, the expected azimuthal dependence in the  $\sigma - \pi'$  channel is

$$I(\psi) = \cos^2(\psi - \delta), \quad (2)$$

and the  $\sigma - \sigma'$  channel has no intensity. This model is shown in Fig. 2(c) with an offset of  $\delta = -5.4^\circ$  and deviates significantly from the data with a large mismatch in periodicity. Both the crystal field around the Ru ion and the canting of its spin can further modulate the azimuthal dependence by lowering the local symmetry of the scattering atom [19]. To better describe the data we included a general, second harmonic term (half the period) that adds a fourfold modulation capturing contributions to the scattering tensor from reduced point symmetry without reference to a specific model:

$$I(\psi) = \{A_1 \cos(\psi - \delta) + A_2 \cos[2(\psi - \delta)]\}^2, \quad (3)$$

where  $A_1$  and  $A_2$  are constants. The second term in Eq. (3) is shown in green in Fig. 2(c) with the same offset. Because of the short range of data, we are unable to evaluate more complex models without a severe overfitting. Nevertheless, we conclude that the  $2\psi$  harmonic term more accurately reproduces the sc110 data. Because in the ns101 film the maximum value of the sinusoid in Fig. 2(d) is inaccessible due to the experimental geometry, the periodicity of the azimuthal dependence in that sample is unconstrained, dependent on rescaling. Fortunately, the position of its minimum near  $90^\circ$  remains informative, since the  $A_2$  term that best approximates the sc110 data achieves a maximum at  $\psi = 90^\circ$  and is thus fully out of phase with the ns101 data. Accordingly, we find Eq. (2) can sufficiently describe the ns101 azimuthal dependence with an offset of  $\delta = 0.7^\circ$ .

The model in Eq. (3) should be interpreted as terms in a Fourier expansion which capture the harmonic content of the azimuthal intensity, irrespective of the underlying physics producing it. The difference in the relative contributions of the two terms arises from differing local symmetry of the scattering center in the two samples. The authors in Ref. [21] identify a fourfold contribution to the azimuthal scan in bulk  $\text{RuO}_2$  with terms corresponding to nonzero components of the magnetization in the  $a$ - $b$  plane, i.e., off  $c$ -axis spin cant-



ing. Similarly, we find that a simple  $\cos^2\psi$  dependence is inadequate to describe sc110. With films mounted in a tilted scattering geometry (Fig. 1), geometric corrections are necessary. At low incidence angle, the beam footprint illuminates a larger volume of the sample increasing the scattered intensity. Furthermore, at low incidence and low exit angle, the beam path through the sample becomes much longer, increasing the effect of self-absorption and lowering the scattered intensity. We have assumed an attenuation length of 600 nm determined by x-ray absorption spectroscopy in Ref. [21]. Finally, the beam spot eventually becomes larger with the dimensions of the samples ( $5 \times 10$  mm) and the measured intensity falls sharply. We have corrected the data to account for all three of these effects, but there remains a possibility for a geometric origin of the deviation from the expected  $\cos^2\psi$  dependence.

Under the assumptions that spin canting is the mechanism modulating the azimuthal intensity and that scattering in the  $\sigma$ - $\sigma'$  channel is vanishing as measured in Ref. [21], then our findings suggest that the high compressive strain in sc110 alters the magnetization direction relative to bulk and bulklike ns101. More recently the conclusion that canting can explain the azimuthal dependence has been called into question [22]. Those authors propose that a chiral signature calculated from all scattering channels is a better indicator of long range antiferromagnetism. Since our experiment used photons with linear incident polarization,  $\sigma$ , we cannot offer support for this claim. Finally, they offer a monoclinic magnetic motif as an alternative to the spin canting, but their model yields the same functional form as Eq. (2) and remains unsatisfactory for both our data and bulk as described in Ref. [22]. Finally, the azimuthal dependence of the 100 peak in  $\text{RuO}_2/\text{STO}$  thin films reported in Ref. [21] is the result of averaging over twin domains, leading to a constant offset and a small amplitude sinusoid with twice the frequency as that of bulk. We emphasize that this mechanism cannot account for the observed periodicity in our azimuthal data, because the film substrates  $\text{TiO}_2(110)$  and  $\text{TiO}_2(101)$  both have different lattice constants in the two in-plane directions, ensuring all domains share a common orientation.

To explore the electronic behavior of magnetic Ru ions in the crystal environment, we measured the photon energy dependence of the magnetic Bragg reflection intensity 100 in the vicinity of the Ru  $L_2$  edge. The averaged energy scans of both films, sc110 and ns101, are shown together in Fig. 3(a) along with data from bulk  $\text{RuO}_2$  redrawn from Ref. [21]. Details of this averaging are shown in Fig. S1 of the Supplemental Material [24]. The double peak shape of the resonance has been previously observed in REXS studies of Ru-based oxides, with the low energy peak corresponding to transitions from  $2p_{1/2}$  core level to  $4d t_{2g}$  orbitals and the high energy peak to transitions into  $4d e_g$  orbitals [21,26,30,32]. The most prominent feature we observe in these resonances is the  $\sim 1$  eV shift of the  $e_g$  peak to higher energy in the superconducting sc110 sample. Notably the  $e_g$  peak only shifts in the sample whose strain induces superconductivity, whereas the resonance profile of differently strained, nonsuperconducting ns101 continues to resemble the bulk profile.

To corroborate the strain dependence of this peak shift, we measured the resonance profile of an identical, (110)-oriented sample, but of greater thickness (48 nm) denoted

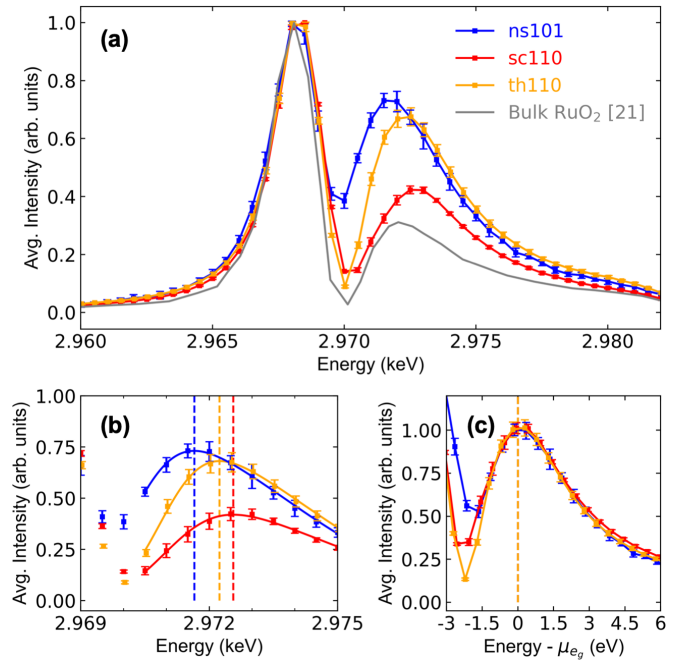


FIG. 3. Strain-tuned resonance profile of the 100 magnetic Bragg peak at the Ru  $L_2$  edge. Panel (a) compares the energy dependence of the normalized, 100 average peak intensity for three  $\text{RuO}_2/\text{TiO}_2$  films: ns101 (18.6 nm, nonsuperconducting, 101 surface normal), sc110 (21 nm, superconducting, 110 surface normal), and th110 (48 nm, nonsuperconducting, 110 surface normal). Data from bulk  $\text{RuO}_2$  are redrawn in gray from Ref. [21]. All curves show a double peak line shape typical of ruthenates with the left peak resulting from transitions into  $t_{2g}$  states and the right peak into  $e_g$  states. Panel (b) enlarges the right peak in (a) and highlights the substantial  $\sim 1$  eV increase of the  $e_g$  peak energy in maximally strained sc110 relative to ns101. The thicker, partially relaxed sample, th110, shows an intermediate peak position and line shape. Solid lines are skewed Gaussian fits to the  $e_g$  peaks with vertical dashed lines indicating the peak positions: 2971.65(1) eV (blue), 2972.24(1) eV (orange), and 2972.56(2) eV (red). Panel (c) shows the same  $e_g$  peaks as in (b) but aligned and rescaled to demonstrate consistency of the line shape and peak width across samples. All scans from film samples are averages over  $N$  measurements ( $N = 17$  for sc110,  $N = 28$  for th110) obtained at 300 K except ns101 ( $N = 12$ ), which is averaged over the range 30–300 K. Error bars are the standard deviation of the  $N$  points at a given photon energy. These resonance profiles have negligible temperature dependence over the range probed (Fig. S1 [24]).

“th110” shown in Fig. 3(a). With increasing thickness, the film does not remain coherently strained throughout its whole extent, and in the case of th110, the lattice relaxes with an average surface lattice constant approaching that of bulk  $\text{RuO}_2$  along [001] and equal to that of bulk along  $[1\bar{1}0]$  determined by low energy electron diffraction (LEED) in Supplemental Material Fig. 14 in Ref. [15]. Transport measurements of th110 reported in Supplemental Material Fig. 11 in Ref. [15] yield a residual resistivity (at 0.45 K) close to the value at 4 K, indicating the absence of bulk superconductivity, yet magnetic suppression of low temperature resistance anomalies suggest an origin in inhomogeneous patches of superconductivity, likely in the coherently strained region.

Characterization of the strain relaxation by scanning transmission electron microscopy (STEM) is also provided in the Supplemental Material of Ref. [15]. For each of the three samples, we fit the  $e_g$  peak with a skewed Gaussian and took the locations of the fitted maxima as the peak positions, shown in Fig. 3(b), yielding a maximum shift of 0.91(3) eV for sc110 and 0.59(3) eV for th110 relative to ns101. More details about the partial relaxation and the fitting procedure are provided in the Supplemental Material [24]. We observe that the increased thickness of th110 leads to a negative shift in energy of its  $e_g$  peak, away from that of the more coherently strained sc110 and more in line with bulk and ns101. This control measurement confirms that strain is the dominant origin for the  $e_g$  energy shift in sc110. We detect no shift in the position of the lower energy  $t_{2g}$  peak between sc110 and ns101. We did not have calibrated photon energy during the th110 measurement, so to correct we shifted its resonance profile by 0.47 eV to align the low energy peak with the other samples in order to compare the shift of its high-energy peak. Moreover, as a result of the inhomogeneous strain relaxation, one may expect broadening of the  $e_g$  profile as vacant electronic states vary in energy across different regions of the film. Normalized and aligned copies of the  $e_g$  peaks for each of the three strain states are shown in Fig. 3(c), with no discernible broadening.

In addition to energy shifts, the relative intensities within the double peak profile vary with strain across samples. We consider the possibility that the variation of the  $e_g$  peak intensity and line shape results from self-absorption. We would expect th110 to exhibit a less intense  $e_g$  peak than sc110 as the former is twice as thick as the latter. The  $e_g$  peak of th110, however, is about 1.5 times taller than that of sc110. Furthermore, the tabulated attenuation lengths for RuO<sub>2</sub> below and above the  $L_2$  edge are approximately 1200 and 900 nm, respectively [21,33]. Further assuming the absorption length decreases to  $\sim 500$  nm on resonance, even in our thickest sample (48 nm), the x-ray intensity would fall by at most 5%, far too small to explain the variation in the  $e_g$  peak intensities we measure. In the 4d transition metal oxides the 2p/4d coupling is of comparable magnitude to the crystal-field splitting and can in turn facilitate the transfer of intensity between the  $t_{2g}$  and  $e_g$  states [32]. The sensitivity of this coupling to Ru-O bond lengths and bond angles suggests a possible explanation of the different  $t_{2g} : e_g$  ratios in the different strain states.

To explain the strain and orbital dependence of the energy scan peak shift, we consider the spatial orientation of the Ru 4d orbitals in the strained, octahedral crystal field shown in Fig. 4(a). In an octahedral crystal field, the  $t_{2g}$  set couples more weakly to the lattice as the lobes of the  $d$  orbitals point toward the faces of the oxygen octahedra leading to weaker  $\pi$  bonding and subsequently reducing their sensitivity to lattice distortions [34]. The lobes of  $e_g$  orbitals point toward the vertices of the octahedra and form antibonding sigma molecular orbitals with the oxygen 2p states. Thus, the  $e_g$  set is more sensitive to changes in bond length with increasing atomic orbital overlap raising the energy of the molecular orbital. Figure 4(a) illustrates displacement of the oxygens toward the  $d_{x^2-y^2}$  and  $d_{z^2}$  orbitals under the strain applied in sc110. Though the oxygens are displaced by +2.3% away from the  $d_{z^2}$  orbital along the  $[1\bar{1}0]$  direction, this relaxation is smaller than the predominant  $c$ -axis compression of  $-4.7\%$ , with the

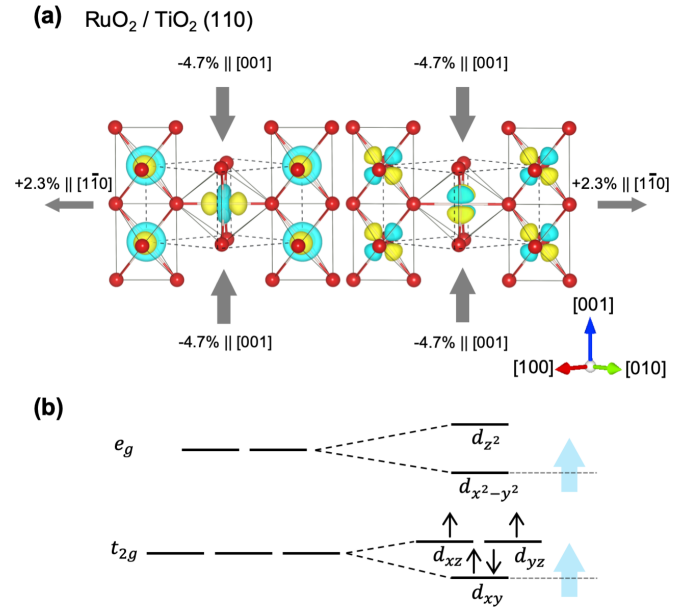


FIG. 4. Schematic depicting the preferential impact of asymmetric epitaxial strain on 4d  $e_g$  orbitals. Panel (a) shows the Ru  $d_{z^2}$  (left) and  $d_{x^2-y^2}$  (right) orbitals within strained oxygen octahedra (red) in the (110)-oriented sample. Gray arrows indicate the strain direction and magnitude. The level splitting in a tetragonally distorted, octahedral crystal field is shown in (b), with blue arrows indicating the shift in energy due to  $c$ -axis compression. Though all level degeneracies are lifted in real RuO<sub>2</sub>, these smaller splittings are suppressed in figure for clarity.

net effect of raising the energy of the  $e_g$  set. The  $d_{x^2-y^2}$  and  $d_{z^2}$  orbitals under  $+2.3\%$   $b$ -axis tension in ns101 are shown in Fig. S4 of the Supplemental Material [24]. While the strain induced in ns101 slightly alters the local symmetry of the crystal field, it does not yield measurable shifts in orbital energies.

The central finding of this work is that the strain state causing large shifts in the energy of the  $e_g$  orbitals is the same one that induces the superconducting ground state at lower temperatures (we were unable to measure the 100 peak at  $T_c$ ). Our ligand-field picture of the  $c$ -axis strain preferentially affecting the  $d_{x^2-y^2}$  states is consistent with *ab initio* modeling of the band structure of the  $t_{2g}$  states under strain [15,16]. In those models shortening the bond length between the ruthenium and equatorial oxygens stabilizes superconductivity by shifting the density of states (DOS) toward the Fermi level, with  $d_{xy}$  and  $d_{x^2-y^2}$  orbitals raised the most in energy [Fig. 4(b)]. This preferential impact of  $c$ -axis compression on the orbitals of  $x^2 - y^2$  and  $xy$  symmetry in sc110 films can also explain the resemblance of ns101 to bulk. Structural relaxation calculations reveal that the net effect of the strain orientation in ns101 is to stretch the apical oxygens away from the ruthenium without impacting equatorial bond lengths, the main drivers of the energy shift [15]. This interpretation is consistent with the observed impact of partial strain relaxation in the 48-nm th110. This film has lost its superconducting transition and displays a more bulklike  $e_g$  peak on resonance. Because the strain relaxation is inhomogeneous with increasing thickness, it is plausible that the energy scan for th110 has blended features of the samples with and without high  $c$ -axis

compression. Without knowing the full strain field in the films, we cannot quantitatively model the magnitude of the  $e_g$  shift as a function of strain nor the expected degree of relaxation in the thickest film.

Ruf *et al.* measured the shifting of density of (occupied) states (mostly  $d_{xy}$  states) toward the Fermi level under increasing  $c$ -axis strain in  $\text{sc110}$  films using angle-resolved photoemission spectroscopy (ARPES) [15], yet we observe no shifts in the  $t_{2g}$  peaks with REXS. In bulk  $\text{RuO}_2$  with its tetragonally distorted (apical oxygens compressed toward the ruthenium) octahedral crystal field, the  $d_{xy}$  states are the lowest in energy and thus predicted to be fully occupied, as shown in Fig. 4(b). Because the REXS energy scan probes empty valence states, it is unsurprising that our data reveal no shift in the lower energy  $t_{2g}$  peak [Fig. 3(a)], as the half-filled orbitals populated during the resonance process,  $d_{yz}$  and  $d_{xz}$ , are those least impacted by the strain field. We conclude the strain-dependent shift in the high energy peak of the Ru  $L_2$  resonance profile is possibly the empty orbital counterpart to the strain-dependent shift in electronic DOS toward the Fermi energy seen with ARPES that drives superconductivity at low temperature.

A similar strain dependence of the crystal-field splitting has been reported in the electron loss near-edge structure (ELNES) of the Ti  $L_3$  edge of  $\text{SrTiO}_3$  [35]. In that experiment, decreasing the net overlap of oxygen  $2p$  orbitals and Ti  $d_{x^2-y^2}$  by distortion of the octahedron shifts the  $e_g$  peak to lower energy while leaving the  $t_{2g}$  unmoved. In the related ferroelectric perovskite  $\text{BaTiO}_3$ , competition between epitaxial strain and polar distortion leads to an atypical crystal-field splitting [36]. Similarly, in (110)-oriented  $\text{RuO}_2$ , we argue that two in-plane strains, compression along  $[001]$  and tension along  $[1\bar{1}0]$ , compete to produce an unconventional crystal-field splitting that shifts the center of gravity of the  $e_g$  manifold to higher energy. This conclusion is further supported by recent work using resonant inelastic x-ray scattering (RIXS) at the Ru  $M$  edge in bulk  $\text{RuO}_2$  [37], uncovering the dominant role of

the reduced symmetry crystal field in determining the orbital energetics.

In summary, we used REXS to study the magnetic Bragg reflection 100 in  $\text{RuO}_2$  in strain-engineered thin films displaying superconductivity at low temperature. We observed modulation of the intensity of the magnetic reflection 100 with azimuth, qualitatively consistent with bulk, but with discrepant periodicities hinting at a strain dependence of the magnetization. Most significantly, we observed a large,  $\sim 1$  eV shift of the  $e_g$  orbitals to higher energy under the same strain state that induces the superconductivity. Relaxation of this  $c$ -axis compression in a thicker, less coherently strained film produced a smaller shift, confirming the strain dependence of the orbital energies. Our measurements of the unoccupied  $e_g$  orbitals show the same trend as *ab initio* modeling of the occupied  $t_{2g}$  states that govern the transport properties of these films and further support the use of anisotropic strains to control physical properties in complex materials. Nevertheless, reconciling whether the large magnitudes of these observed shifts can be accounted for solely by strain effects remains to be clarified in future work (both experimental and computational).

We acknowledge helpful conversations with C. A. Occhialini and J. Pellicciari. The work was primarily supported by U.S. Department of Energy, Office of Science, Office of Basic Energy Sciences, under Contract No. DE-SC0019414 (x-ray experiments and interpretation: B.Z.G., D.W., Y.S., A.S.; thin film synthesis: H.N., N.J.S.). This research used resources of the Advanced Photon Source, a U.S. Department of Energy (DOE) Office of Science User Facility operated for the DOE Office of Science by Argonne National Laboratory under Contract No. DE-AC02-06CH11357. This work was also funded in part by the Gordon and Betty Moore Foundation's EPIQS Initiative, Grant No. GBMF9073 to Cornell University to support the work of D.G.S., and NSF Grants No. DMR-2104427 and No. AFOSR FA9550-21-1-0168 (characterization and model development: J.P.R., K.M.S.).

- 
- [1] Y. Maeno, H. Hashimoto, K. Yoshida, S. Nishizaki, T. Fujita, J. G. Bednorz, and F. Lichtenberg, *Nature (London)* **372**, 532 (1994).
  - [2] R. S. Perry, L. M. Galvin, S. A. Grigera, L. Capogna, A. J. Schofield, A. P. Mackenzie, M. Chiao, S. R. Julian, S. Ikeda, S. Nakatsuji, Y. Maeno, and C. Pfleiderer, *Phys. Rev. Lett.* **86**, 2661 (2001).
  - [3] K. Kitagawa, K. Ishida, R. S. Perry, T. Tayama, T. Sakakibara, and Y. Maeno, *Phys. Rev. Lett.* **95**, 127001 (2005).
  - [4] Y. Tokiwa, M. McHalwat, R. S. Perry, and P. Gegenwart, *Phys. Rev. Lett.* **116**, 226402 (2016).
  - [5] N. Nakatsuji, S.-I. Ikeda, and Y. Maeno, *J. Phys. Soc. Jpn.* **66**, 1868 (1997).
  - [6] Y. Yoshida, S.-I. Ikeda, H. Matsuhata, N. Shirakawa, C. H. Lee, and S. Katano, *Phys. Rev. B* **72**, 054412 (2005).
  - [7] J. Bertinshaw, M. Krautloher, H. Suzuki, H. Takahashi, A. Ivanov, H. Yavaş, B. J. Kim, H. Gretarsson, and B. Keimer, *Phys. Rev. B* **103**, 085108 (2021).
  - [8] J. M. Longo, P. M. Raccach, and J. B. Goodenough, *J. Appl. Phys.* **39**, 1327 (1968).
  - [9] *Frontiers of 4d- and 5d-Transition Metal Oxides*, edited by G. Cao and L. De-Long (World Scientific, Singapore, 2013).
  - [10] A. Steppke, L. Zhao, M. E. Barber, T. Scaffidi, F. Jerzembeck, H. Rosner, A. S. Gibbs, Y. Maeno, S. H. Simon, A. P. Mackenzie, and C. W. Hicks, *Science* **355**, eaaf9398 (2017).
  - [11] B. Burganov, C. Adamo, A. Mulder, M. Uchida, P. D. C. King, J. W. Harter, D. E. Shai, A. S. Gibbs, A. P. Mackenzie, R. Uecker, M. Bruetzlam, M. R. Beasley, C. J. Fennie, D. G. Schlom, and K. M. Shen, *Phys. Rev. Lett.* **116**, 197003 (2016).
  - [12] S.-I. Ikeda, N. Shirakawa, T. Yanagisawa, Y. Yoshida, S. Koikegami, S. Koike, M. Kosaka, and Y. Uwatoko, *J. Phys. Soc. Jpn.* **73**, 1322 (2004).
  - [13] A. J. Grutter, F. J. Wong, E. Arenholz, A. Vailionis, and Y. Suzuki, *Phys. Rev. B* **85**, 134429 (2012).
  - [14] A. Grutter, F. Wong, E. Arenholz, M. Liberati, and Y. Suzuki, *J. Appl. Phys.* **107**, 09E138 (2010).

- [15] J. P. Ruf, H. Paik, N. J. Schreiber, H. P. Nair, L. Miao, J. K. Kawasaki, J. N. Nelson, B. D. Faeth, Y. Lee, B. H. Goodge, B. Pamuk, C. J. Fennie, L. F. Kourkoutis, D. G. Schlom, and K. M. Shen, *Nat. Commun.* **12**, 59 (2021).
- [16] M. Uchida, T. Nomoto, M. Musashi, R. Arita, and M. Kawasaki, *Phys. Rev. Lett.* **125**, 147001 (2020).
- [17] W. D. Ryden and A. W. Lawson, *J. Chem. Phys.* **52**, 6058 (1970).
- [18] T. Berlijn, P. C. Snijders, O. Delaire, H. D. Zhou, T. A. Maier, H. B. Cao, S. X. Chi, M. Matsuda, Y. Wang, M. R. Koehler, P. R. C. Kent, and H. H. Weitering, *Phys. Rev. Lett.* **118**, 077201 (2017).
- [19] M. W. Haverkort, N. Hollmann, I. P. Krug, and A. Tanaka, *Phys. Rev. B* **82**, 094403 (2010).
- [20] J. Fink, E. Schierle, E. Weschke, and J. Geck, *Rep. Prog. Phys.* **76**, 056502 (2013).
- [21] Z. H. Zhu, J. Strempler, R. R. Rao, C. A. Occhialini, J. Pellicciari, Y. Choi, T. Kawaguchi, H. You, J. F. Mitchell, Y. Shao-Horn, and R. Comin, *Phys. Rev. Lett.* **122**, 017202 (2019).
- [22] S. W. Lovesey, D. D. Khalyavin, and G. van der Laan, *Phys. Rev. B* **105**, 014403 (2022).
- [23] A. Bose, N. J. Schreiber, R. Jain, D.-F. Shao, H. P. Nair, J. Sun, X. S. Zhang, D. A. Muller, E. Y. Tsybal, D. G. Schlom, and D. C. Ralph, *Nat. Electron.* **5**, 267 (2022).
- [24] See Supplemental Material at <http://link.aps.org/supplemental/10.1103/PhysRevB.106.195135> for further description of sample characterization and details of analysis.
- [25] J. K. Burdett, T. Hughbanks, G. J. Miller, J. W. Richardson, and J. V. Smith, *J. Am. Chem. Soc.* **109**, 3639 (1987).
- [26] B. Bohnenbuck, I. Zegkinoglou, J. Strempler, C. S. Nelson, H.-H. Wu, C. Schüssler-Langeheine, M. Reehuis, E. Schierle, P. Leininger, T. Herrmannsdörfer, J. C. Lang, G. Srajer, C. T. Lin, and B. Keimer, *Phys. Rev. Lett.* **102**, 037205 (2009).
- [27] B. Bohnenbuck, I. Zegkinoglou, J. Strempler, C. Schüssler-Langeheine, C. S. Nelson, P. Leininger, H.-H. Wu, E. Schierle, J. C. Lang, G. Srajer, S. I. Ikeda, Y. Yoshida, K. Iwata, S. Katano, N. Kikugawa, and B. Keimer, *Phys. Rev. B* **77**, 224412 (2008).
- [28] M. A. Hossain, I. Zegkinoglou, Y.-D. Chuang, J. Geck, B. Bohnenbuck, A. G. C. Gonzalez, H.-H. Wu, C. Schüssler-Langeheine, D. G. Hawthorn, J. D. Denlinger, R. Mathieu, Y. Tokura, S. Satow, H. Takagi, Y. Yoshida, Z. Hussain, B. Keimer, G. A. Sawatzky, and A. Damascelli, *Sci. Rep.* **3**, 2299 (2013).
- [29] D. G. Porter, V. Granata, F. Forte, S. Di Matteo, M. Cuoco, R. Fittipaldi, A. Vecchione, and A. Bombardi, *Phys. Rev. B* **98**, 125142 (2018).
- [30] I. Zegkinoglou, J. Strempler, C. S. Nelson, J. P. Hill, J. Chakhalian, C. Bernhard, J. C. Lang, G. Srajer, H. Fukazawa, S. Nakatsuji, Y. Maeno, and B. Keimer, *Phys. Rev. Lett.* **95**, 136401 (2005).
- [31] J. P. Hannon, G. T. Trammell, M. Blume, and D. Gibbs, *Phys. Rev. Lett.* **61**, 1245 (1988).
- [32] Z. Hu, H. von Lips, M. S. Golden, J. Fink, G. Kaindl, F. M. F. de Groot, S. Ebbinghaus, and A. Reller, *Phys. Rev. B* **61**, 5262 (2000).
- [33] B. L. Henke, E. M. Gullikson, and J. C. Davis, *At. Data Nucl. Data Tables* **54**, 181 (1993).
- [34] C. J. Ballhausen, *Introduction to Ligand Field Theory* (McGraw Hill Book Co., Inc, New York, 1962).
- [35] D. Ávila-Brandé, M. Boese, L. Houben, J. Schubert, and M. Luysberg, *ACS Appl. Mater. Interfaces* **3**, 1545 (2011).
- [36] Y. Song, X. Liu, F. Wen, M. Kareev, R. Zhang, Y. Pei, J. Bi, P. Shafer, A. T. N'Diaye, E. Arenholz, S. Y. Park, Y. Cao, and J. Chakhalian, *Phys. Rev. Mater.* **4**, 024413 (2020).
- [37] C. A. Occhialini, V. Bisogni, H. You, A. Barbour, I. Jarrige, J. F. Mitchell, R. Comin, and J. Pellicciari, *Phys. Rev. Res.* **3**, 033214 (2021).